A Theory of Topographically Bound Balanced Motions and Application to Atmospheric Low-Level Jets

LEVI G. SILVERS* AND WAYNE H. SCHUBERT

Colorado State University, Fort Collins, Colorado

ABSTRACT

The subject of this study is topographically bound low-level jets, such as the South American summertime low-level jet on the eastern side of the Andes and its companion, the Chilean low-level jet on the western side of the Andes. These jets are interpreted as balanced flows that obey the potential vorticity invertibility principle. This invertibility principle is expressed in isentropic coordinates, and the mathematical issue of isentropes that intersect the topography is treated by the method of a massless layer. In this way, the low-level jets on the western and eastern sides of the Andes can both be attributed to the infinite potential vorticity that lies in the infinitesimally thin massless layer on the topographic feature. To obtain a cyclonic flow centered on the topographic feature, the mountain crest must have been heated enough to draw down the overlying isentropic surfaces; otherwise, isentropic surfaces bend upward at the mountain crest and an anticyclonic flow is produced. Both anticyclonic and cyclonic solutions are obtained here using analytical and numerical methods to solve the invertibility principle. The summertime topographically bound flows discussed here are quite distinct from the wintertime Rossby wave train patterns that occur when strong westerlies impinge on the topography.

1. Introduction

Figure 1 shows the 1 December 2009 to 31 January 2010 mean winds at 925 hPa in the region of South America. A striking feature of Fig. 1 is the strong cyclonic flow centered on the Andes. The South American low-level jet (SALLJ) is evident in the northerly flow east of the Andes, while the Chilean coastal low-level jet is evident in the southerly flow over the eastern Pacific Ocean. These Southern Hemisphere low-level jets (LLJs) are analogous to the summertime low-level jets around the mountainous regions of North America, that is, the Great Plains low-level jet (GPLLJ) and the California coastal low-level jet. That there is a cyclonic circulation centered on both the Rockies and the Andes suggests the possibility of a common dynamical link between the prevalent low-level jets of North and South America.

Figures 2 and 3 show east–west cross sections of the 2-month mean meridional wind fields and the mean

isentropes observed over the Rockies and the Andes. Figures 1–3 were constructed using Year of Tropical Convection (YOTC) analysis [as described by Waliser et al. (2012)]. The time resolution of these European Centre for Medium-Range Weather Forecasts analysis fields is 6 h and the horizontal resolution is $0.5° \times 0.5°$ with 15 irregularly spaced vertical levels. The YOTC analysis is available for the 2-yr period between May 2008 and April 2010. Although originally proposed to be a 1-yr research program, YOTC was extended for an additional year in order to capture both La Niña and El Niño phases of an ENSO cycle. Wind fields around the Andes are shown at 21° and 30°S. The SALLJ often maximizes near 20°S while, as seen in Fig. 2, the coastal LLJ is stronger farther south. Cross sections of the wind fields around the Rocky Mountains are shown at 30° and 35°N. The GPLLJ maximizes at about 25°N but, as seen in Fig. 3, it is still quite strong at 30° and 35°N. The coastal LLJs tend to have a wind maximum closer to the surface than the jets to the east of the mountain ranges. The coastal jets are also broader than the plains jets partly because of the influence of the Pacific anticyclonic circulations to the west. Isentropes are generally drawn down over the mountain ranges, thereby intersecting the earth's surface along the sides and crests of the mountains. It should be noted that, on individual days, these

---

* Current affiliation: Max Planck Institute for Meteorology, Hamburg, Germany.

Corresponding author address: Levi Silvers, Max Planck Institute for Meteorology, Bundesstrasse 53, 20146 Hamburg, Germany.
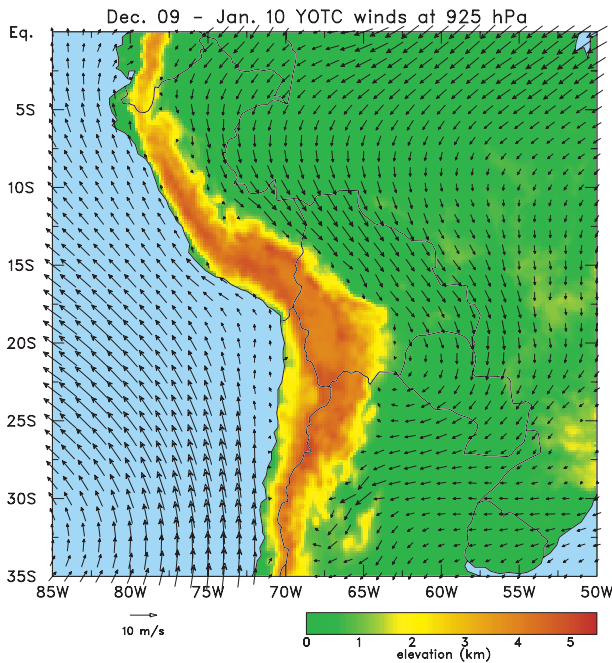E-mail: levi.silvers@zmaw.de

FIG. 1. Two-month mean 925-hPa wind (10 m s⁻¹ vector indicated just left of the color bar) from the YOTC analysis data. This mean has been computed by averaging analysis data with a time resolution of 6 h, so diurnal variability has been smoothed. Vectors are not drawn in the region of the Andes above 925 hPa. The background map shows topography (see color bar). The horizontal resolution of the YOTC analysis is $0.5° \times 0.5°$, but for clarity only $1° \times 1°$ wind data are plotted here.

low-level jets can be considerably stronger than shown on 2-month mean cross sections. For example, Vera et al. (2006, their Fig. 8b) show a specific SALLJ event in February 2003 with a maximum wind of 25 m s⁻¹ at a height of 800–700 hPa. The cyclonic motion centered on the mountain ranges is the most obvious feature of the wind fields in these figures. The North American Regional Reanalysis also clearly shows a dominant cyclonic circulation (see Jiang et al. 2007, their Fig. 1) over the Rocky Mountains. We have also constructed cross sections (not shown) like Figs. 2 and 3 for the meridional geostrophic wind. The meridional geostrophic wind fields are noisier than the fields shown in Figs. 2 and 3 because the zonal pressure gradient force is computed from geopotential fields interpolated to isobaric surfaces from the ECMWF hybrid vertical coordinate data. In spite of this practical difficulty, the cross sections confirm that the topographically bound low-level flows can be regarded as essentially geostrophic flows.

One of the first climatologies of LLJs was given by Bonner (1968), along with an often used set of wind shear criteria to define LLJs. Stensrud (1996) provided a review of LLJs and, in particular, their significant influence on the global climate. An excellent review of
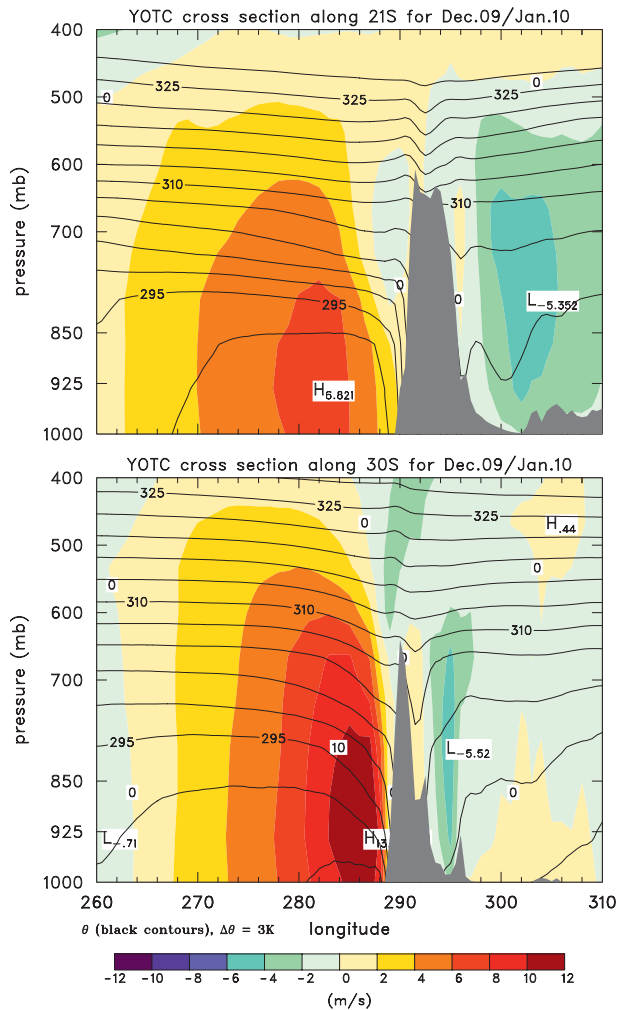

FIG. 2. Mean warm season cross section of meridional wind at (top) 21°S and (bottom) 30°S from the ECMWF (see text) YOTC data. The magnitude of the meridional wind is given by the color bar; black contours are isentropes. YOTC data are available at the levels 100, 150, 200, 250, 300, 400, 500, 600, 700, 800, 850, 900, 925, 950, and 1000 hPa, but only the 10 data levels between 400 and 1000 hPa are used in this cross section and in Fig. 3.

the literature relevant to LLJs and analysis of the dynamical mechanisms that have been historically proposed to explain the existence and variability of LLJs was given by Jiang et al. (2007). Much of the previous research on LLJs can be loosely grouped into two categories. The first includes boundary layer processes and forcing on relatively short (diurnal to a few days) time scales. Relevant studies include Blackadar (1957), Holton (1967), Jiang et al. (2007), and Rife et al. (2010). These studies were particularly interested in determining the physical mechanisms behind the diurnal oscillation that is observed in many LLJs. The second category deals mostly with the synoptic-scale monthly or seasonal mean structure of LLJs and includes studies such as Wexler (1961),
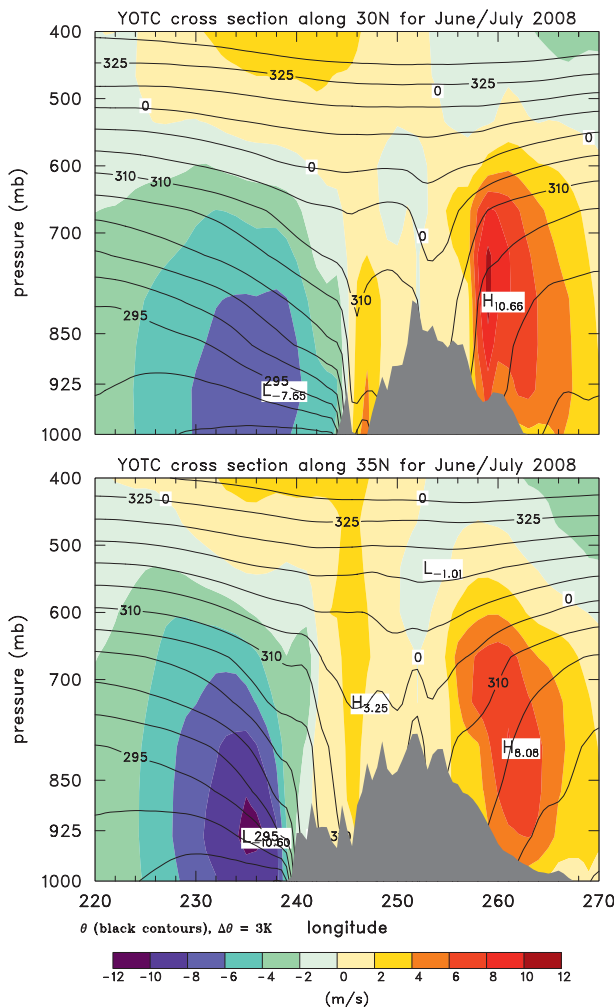
FIG. 3. Mean warm season cross section of meridional wind field at (top) 30°N and (bottom) 35°N from the ECMWF YOTC data. The magnitude of wind is given by the color bar; black contours are isentropes.

Byerle and Paegle (2002, 2003), and Ting and Wang (2006). These two groups certainly have some overlap. The research presented here interprets LLJs as synoptic-scale topographically bound balanced motions attributable, through the potential vorticity invertibility principle, to the heating of elevated terrain.

The theoretical study most relevant to the present work is that of Eliassen (1980), who investigated the steady, topographically bound, balanced response of a rotating, stratified fluid to orography. Although Eliassen did not specifically apply his theory to LLJs, his results provide physical insight into the dynamical characteristics of these phenomena. Eliassen defined isentropic obstacles as those for which the lowermost isentrope continuously follows the topographic surface. A nonisentropic obstacle is one for which the topographic surface punctures the

lowermost isentropes. Eliassen showed that solutions of the potential vorticity invertibility principle for an isentropic ridge were only possible if the height of that ridge did not exceed its critical value. This "subcritical ridge" case is illustrated by the left panel of Fig. 4, which shows that the isentropes are compressed as they bend up over the mountain crest, thereby producing a balanced anticyclonic flow above the crest. If the "critical crest height" is exceeded, the ridge must puncture the lowermost isentropes. Two other cases not investigated by Eliassen are shown in the middle and right panels of Fig. 4. The middle panel shows a surface of constant geopotential that has been locally heated. In this case the isentropes bend downward and a balanced, cyclonic flow is produced. The surface potential temperature anomaly shown in the middle panel of Fig. 4 represents a balanced flow structure similar to those studied by Hoskins et al. (1985) and Thorpe (1986). Their work solved an isobaric coordinate form of the invertibility principle for synoptic disturbances in gradient wind balance, whereas the present study solves the isentropic coordinate form of the invertibility principle for synoptic disturbances in geostrophic balance. A combination of the two cases shown in the left and middle panels of Fig. 4 results in the heated obstacle shown in the right panel. Clearly, the right panel is the case most relevant to the observations shown in Figs. 1–3.

The purpose of the present paper is to extend the analysis of Eliassen to include all three cases shown in Fig. 4 and thereby demonstrate that many LLJs can be interpreted as balanced flows attributed, through the potential vorticity invertibility principle, to the infinite potential vorticity that resides in the massless layer over locally heated topography such as illustrated in the right panel of Fig. 4. A complete potential vorticity analysis of LLJs would have to include both the potential vorticity at the surface that results from a gradient of surface potential temperature and any potential vorticity anomalies that reside in the interior. The surface component is related to surface radiative heating while the interior component is due to convective activity that produces nonuniform potential vorticity along interior isentropic surfaces. The interaction between the interior potential vorticity and the surface gradient of potential temperature was reviewed by Hoskins et al. (1985). A nongeostrophic generalization was applied to a wake circulation on the lee side of a mountain by Schneider et al. (2003). We here focus on the surface potential temperature variation. We do not wish to imply that the effect of the surface potential temperature variation is greater than that of the interior potential vorticity anomalies in all cases, but rather that an important part of the LLJ response is related to this surface potential temperature variation.
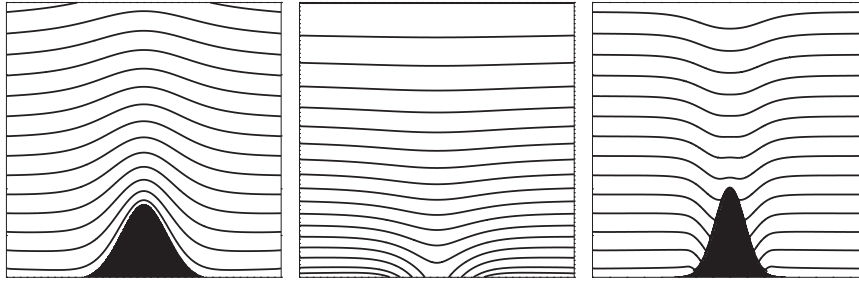
FIG. 4. Schematic vertical cross sections representing the three idealized configurations studied here. Contours represent lines of constant potential temperature (isentropes), with the vertical axes interpreted as height. (left) An isentropic obstacle, (middle) a heated flat lower surface, and (right) a heated obstacle.

The outline of the paper is as follows. Section 2 presents the *f*-plane invertibility principle in isentropic coordinates. Section 3 derives analytical solutions for the subcritical isentropic ridge case. An analytical formula for the critical crest height is then derived. The analytical methods used in section 3 yield closed form solutions only in cases where there is no massless layer (i.e., the lower boundary is an isentropic surface). To compute the wind and mass fields that result from locally heated lower boundaries, section 4 solves the invertibility principle using a finite-difference approximation. An analysis is then made of the results and how they compare to observations of LLJs. Concluding remarks, including a discussion of a generalization from *f*-plane theory to the sphere, are given in section 5.

2. Invertibility principle

Consider hydrostatic, geostrophic, *y*-independent motions of a compressible stratified fluid on an *f* plane. Using the potential temperature θ as the vertical coordinate, the potential vorticity is given by

$$P = \left(f + \frac{\partial v}{\partial x}\right)\left(-\frac{1}{g}\frac{\partial p}{\partial \theta}\right)^{-1}, \tag{1}$$

with *f* denoting the constant Coriolis parameter, *g* the acceleration of gravity, $v(x, \theta)$ the meridional component of the geostrophic flow, and $p(x, \theta)$ the pressure. Expressing the density by $\rho = p/(RT) = c_p p/(R\theta\Pi)$, it is easily shown that $\theta\rho(d\Pi/dp) = 1$, where $\Pi = c_p(p/p_0)^{R/c_p}$ with p_0 denoting the constant reference pressure, *R* the gas constant, and c_p the specific heat at constant pressure. This allows (1) to be written in the form

$$\frac{g}{\theta\rho P}\left(f + \frac{\partial v}{\partial x}\right) + \frac{\partial \Pi}{\partial \theta} = 0. \tag{2}$$

Using the geostrophic relation $fv = (\partial M/\partial x)$ and the hydrostatic relation $\Pi = (\partial M/\partial \theta)$, where $M = \theta\Pi + \phi$ is

the Montgomery potential and ϕ is the geopotential, we can write the thermal wind relation in the form

$$f\frac{\partial v}{\partial \theta} - \frac{\partial \Pi}{\partial x} = 0. \tag{3}$$

With proper boundary conditions and with $P(x, \theta)$ specified, (2) and (3) constitute an invertibility problem for the unknown functions $v(x, \theta)$ and $\Pi(x, \theta)$. Because of the dependence of ρ on Π, (2) is nonlinear. However, the nonlinearity is weak and, for the analytical solutions presented in section 3, it will be removed by replacing $\rho(x, \theta)$ with the specified far-field profile $\tilde{\rho}(\theta)$. For the numerical solutions presented in section 4, this nonlinearity will be retained.

3. Analytical solution for the case of an isentropic mountain

For the analytical results presented in this section it is preferable to work with deviations from the far-field values. In the far field the flow vanishes, and the pressure and potential vorticity take on the horizontally homogeneous values $\tilde{p}(\theta)$ and $\tilde{P}(\theta)$, which are related by

$$\tilde{P} = f\left(-\frac{1}{g}\frac{\partial \tilde{p}}{\partial \theta}\right)^{-1}. \tag{4}$$

Denoting the far-field density by $\tilde{\rho}(\theta)$, it is easily shown that $\theta\tilde{\rho}(d\tilde{\Pi}/d\tilde{p}) = 1$, where $\tilde{\Pi} = c_p(\tilde{p}/p_0)^{R/c_p}$. This allows (4) to be written in the form

$$\frac{gf}{\theta\tilde{\rho}\tilde{P}} + \frac{\partial \tilde{\Pi}}{\partial \theta} = 0. \tag{5}$$

Taking the difference of (2) and (5), we obtain

$$\frac{\tilde{\rho}\tilde{P}}{\rho P}\frac{\partial v}{\partial x} + \left(\frac{f\theta^2 N^2}{g^2}\right)\frac{\partial \Pi'}{\partial \theta} = f\left(1 - \frac{\tilde{\rho}\tilde{P}}{\rho P}\right), \tag{6}$$

where $\Pi'(x, \theta) = \Pi(x, \theta) - \tilde{\Pi}(\theta)$ is the Exner function anomaly, and where the buoyancy frequency $N(\theta)$ is defined by

$$N^2(\theta) \equiv \frac{g^2}{\theta^2}\left(-\frac{d\tilde{\Pi}}{d\theta}\right)^{-1}. \qquad (7)$$

In the analysis of this section, four simplifying assumptions are made: (i) the lower boundary is assumed to be an isentropic surface; (ii) the factors $(\tilde{\rho}/\rho)$ in (6) are approximated by unity; (iii) on each isentropic surface the potential vorticity P is assumed to be equal to its far-field value $\tilde{P}$ so that the right-hand side (rhs) of (6) vanishes and the coefficient of $(\partial v/\partial x)$ becomes unity; and (iv) the reference state buoyancy frequency $N(\theta)$ is assumed to be inversely proportional to θ, that is, $N(\theta) = N_B\theta_B/\theta$, where N_B and θ_B are constants, which results in a constant coefficient for the second term in (6). In the numerical calculations presented in section 4, only the assumption concerning the vertical profile of $N(\theta)$ will be retained. In particular, the lower boundary will not be an isentrope, and the potential vorticity will not be uniform on those isentropes that intersect the lower boundary, although we will still assume the potential vorticity is uniform on those isentropes that do not intersect the lower boundary. Thus, the present work considers only those balanced flows associated with surface processes, and not balanced flows associated with interior potential vorticity anomalies. However, it should be noted that cumulus convection and convective turbulence over elevated terrain will result in interior potential vorticity anomalies and associated balanced flows that are not considered here.

For the particular reference state $N(\theta) = N_B\theta_B/\theta$, the definition (7) can be integrated to obtain

$$\tilde{\Pi}(\theta) = c_p - \frac{g^2}{\theta_B^2 N_B^2}(\theta - \theta_B), \qquad (8)$$

where $\tilde{p}(\theta_B) = p_0$. The reference state hydrostatic equation $d\tilde{M}/d\theta = \tilde{\Pi}$ can then be integrated to obtain

$$\tilde{M}(\theta) = c_p\theta - \frac{g^2}{2\theta_B^2 N_B^2}(\theta - \theta_B)^2, \qquad (9)$$

where we have assumed $\tilde{\phi}(\theta_B) = 0$. Since $\tilde{\phi}(\theta) = \tilde{M}(\theta) - \theta\tilde{\Pi}(\theta)$, we can use (8) and (9) to obtain

$$\tilde{\phi}(\theta) = \frac{g^2}{2\theta_B^2 N_B^2}(\theta^2 - \theta_B^2). \qquad (10)$$

The relationship of pressure and potential temperature for the reference state, as determined from (8), is plotted in
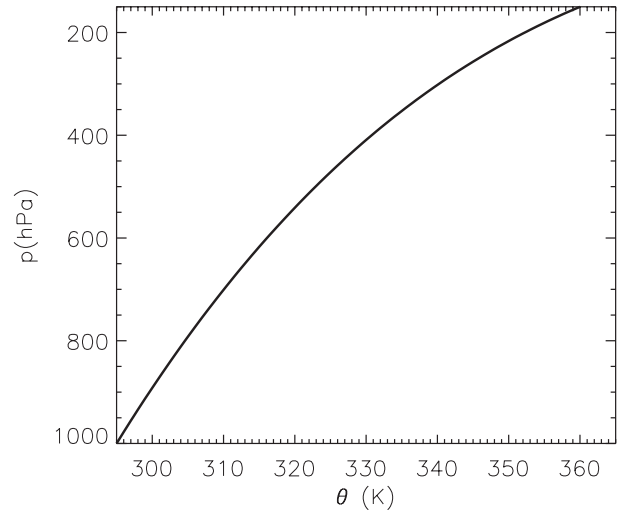

FIG. 5. Reference pressure $\tilde{p}$ as a function of θ, computed from (8).

Fig. 5, where we have chosen $c_p = 1004.5$ J kg^{-1} K^{-1}, $g = 9.8$ m s^{-2}, $\theta_B = 295$ K, and $(\theta_B/g)N_B^2 = 5.1373$ K km^{-1}. This choice of θ_B and N_B results in a profile with $\tilde{p}(\theta) = 150$ hPa at $\theta = 360$ K. The associated value of N_B is 1.3064×10^{-2} s^{-1}. For the model top, the value $\theta_T = 360$ K is used throughout this study. Although idealized, this reference state profile, with $\theta = 331$ K at 400 hPa and $\theta = 295$ K at 1000 hPa, can be considered typical of the profiles found at different locations in Figs. 2 and 3, noting of course that the actual values of θ on the lower boundary in Figs. 2 and 3 have a relatively wide range because of the contrast between the cold ocean and the warm continent.

With the four simplifying assumptions listed above, the Cauchy–Riemann conditions (6) and (3) simplify to (11) and (12) below. We shall require that (11) and (12) hold in a region that includes an underlying topographic feature whose geopotential is specified by $\phi_S(x)$. As for boundary conditions, we require that v and Π' approach zero in the far field, which is expressed in (13). We also require that the upper boundary is both an isentropic ($\theta = \theta_T$) and isobaric surface, which is expressed as (14). To formulate the lower boundary condition we combine the x derivative of $M - \theta\Pi = \phi$ with the geostrophic and hydrostatic relations to obtain $f[v - \theta(\partial v/\partial\theta)] = (\partial\phi/\partial x)$, which, when applied at $\theta = \theta_B$, yields (15). In summary, the elliptic problem is

$$\frac{\partial v}{\partial x} + \left(\frac{f\theta_B^2 N_B^2}{g^2}\right)\frac{\partial\Pi'}{\partial\theta} = 0, \qquad (11)$$

$$f\frac{\partial v}{\partial\theta} - \frac{\partial\Pi'}{\partial x} = 0, \qquad (12)$$

with boundary conditions

$$v \to 0 \quad \text{and} \quad \Pi' \to 0 \quad \text{as} \quad x \to \pm\infty, \quad (13)$$

$$\Pi' = 0 \quad \text{at} \quad \theta = \theta_T, \quad (14)$$

$$f\left(v - \theta \frac{\partial v}{\partial \theta}\right) = \frac{d\phi_S(x)}{dx} \quad \text{at} \quad \theta = \theta_B. \quad (15)$$

This elliptic problem can be solved using Fourier integral transforms. The details can be found in the appendix. For

all calculations presented in this paper we have chosen the geopotential on the lower boundary as

$$\phi_S(x) = gHe^{-x^2/a^2}, \quad (16)$$

where the constants H and a respectively specify the mountain height and width. The final solutions for the balanced wind and mass fields are

$$v(x,\theta) = -\frac{gHa}{f\sqrt{\pi}}\int_0^\infty ke^{-a^2k^2/4}\left[\frac{e^{-\kappa(\theta-\theta_B)} + e^{-\kappa(2\theta_T-\theta_B-\theta)}}{1 + \kappa\theta_B + (1 - \kappa\theta_B)e^{-2\kappa(\theta_T-\theta_B)}}\right]\sin(kx)\, dk, \quad (17)$$

$$\Pi'(x,\theta) = -\frac{g^2Ha}{f\theta_B N_B\sqrt{\pi}}\int_0^\infty ke^{-a^2k^2/4}\left[\frac{e^{-\kappa(\theta-\theta_B)} - e^{-\kappa(2\theta_T-\theta_B-\theta)}}{1 + \kappa\theta_B + (1 - \kappa\theta_B)e^{-2\kappa(\theta_T-\theta_B)}}\right]\cos(kx)\, dk, \quad (18)$$

where k is the horizontal wavenumber and $\kappa = gk/(f\theta_B N_B)$. Equations (17) and (18) are the Fourier integral representations of the solutions to the invertibility problem (11)–(15). Plots of the solutions $v(x, \theta)$ and $\Pi'(x, \theta)$ are easily constructed through numerical evaluation of the Fourier integrals at each point of an array of points in (x, θ) space. In the construction of several of the figures shown here, we have chosen to display isolines of v and θ in (x, p) space in addition to isolines of v and p in (x, θ) space. Conversion between these two representations is simply a matter of interpolation.

Figure 6 shows a plot of the solutions $v(x, p)$ and $\theta(x, p)$ for $f = 7.3 \times 10^{-5}$ s^{-1}, $a = 500$ km, and $H = 1500$ m. Figure 7 shows a similar plot with $H = 2500$ m. As can be seen from Fig. 7, when $H = 2500$ m the layer $295 \le \theta \le 296$ K is almost massless near the mountain crest. In fact, for H greater than 2560 m, this layer does become massless at the mountain crest. In other words, for this

particular mountain shape and far-field reference state, the critical crest height is approximately $H_{\text{crit}} = 2560$ m. Following an argument similar to that of Eliassen (1980), a formula for the critical height can be obtained as follows. When $H = H_{\text{crit}}$, $(\partial\Pi/\partial\theta) = (\partial\tilde{\Pi}/\partial\theta) + (\partial\Pi'/\partial\theta) = 0$ at the crest, or equivalently, using (8),

$$\frac{\partial\Pi'}{\partial\theta} = \frac{g^2}{\theta_B^2 N_B^2} \quad \text{at} \quad x = 0 \quad \text{and} \quad \theta = \theta_B. \quad (19)$$

Using (18) for Π', with H replaced by H_{crit}, we can rewrite (19) as

$$H_{\text{crit}} = \frac{fa}{N_B I(a)}, \quad (20)$$

where

$$I(a) = \frac{1}{\sqrt{\pi}}\int_0^\infty \left(\frac{\hat{a}^2\hat{\kappa}^2\{1 + \exp[-2\hat{\kappa}(\theta_T - \theta_B)/\theta_B]\}}{1 + \hat{\kappa} + (1 - \hat{\kappa})\exp[-2\hat{\kappa}(\theta_T - \theta_B)/\theta_B]}\right)\exp(-\hat{a}^2\hat{\kappa}^2/4)\, d\hat{\kappa}, \quad (21)$$

with $\hat{a} = (fN_B/g)a$ denoting the dimensionless mountain width and with $\hat{\kappa} = \kappa\theta_B$. Figure 8 shows H_{crit} as a function of a for five different values of f. These results indicate that broad mountains can be relatively high but still below the critical crest height. They also indicate that the crest height of the central Andes is supercritical. For example, the actual crest heights shown in the two panels of Fig. 2 are approximately 4200 m (at 21°S) and 3700 m (at 30°S), both of which are considerably higher than the critical crest heights from the two curves labeled 20° and 30° latitude in Fig. 8.

In concluding this section we note that the wind and mass fields displayed in Figs. 6 and 7 can also be interpreted as solutions of the following geostrophic adjustment problem (Eliassen 1980). Initially, a stably stratified fluid is in a state of rest over a level bottom surface on an f plane. Over some arbitrary time interval, the bottom topography is raised to its final shape and any transient inertia–gravity waves are allowed to disperse away. The final adjusted wind and mass fields are then determined via the potential vorticity invertibility principle (11)–(15), with the bottom topography appearing in the
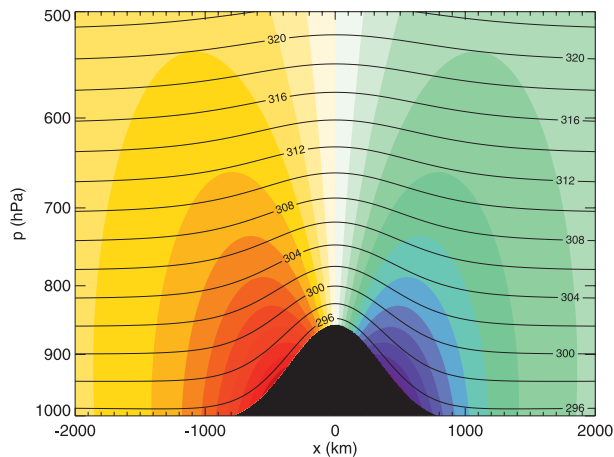
FIG. 6. Cross-section plot of meridional wind v (shading) and potential temperature θ (solid lines) computed near a Gaussian isentropic mountain with "width" $a = 500$ km and crest height $H = 1500$ m. The potential temperature on the mountain surface is 295 K, and the flow is anticyclonic. The contour intervals are 1 m s^{-1} for v and 2 K for θ. The extreme values of v are $+11.5$ m s^{-1} on the western side (dark red) of the mountain and -11.5 m s^{-1} on the eastern side (dark blue).

FIG. 7. As in Fig. 6, but with crest height $H = 2500$ m. The peak values of v are ±19.2 m s^{-1}.

lower boundary condition of this invertibility principle. If the crest height of the topography is not raised above the critical value, the lowest isentropic surface remains attached to the topography. However, if the crest of the topography is raised above the critical value, the topography punctures the lowest isentropic surfaces so that potential temperature now varies along the lower boundary. In either case, the flow around the obstacle is anticyclonic, a result of Coriolis turning of fluid that flows away from the rising mountain crest. This anticyclonic, topographically bound, balanced flow is not useful for describing cyclonic flows such as those shown in Figs. 1–3. Thus, in the next section we consider the related problem of the balanced wind and mass fields near a topographic feature that has been heated by radiative processes, resulting in a cyclonic flow around the obstacle. This will allow us to interpret the South American low-level jet and the Chilean low-level jet as parts of the topographically bound motion associated with the PV anomaly produced by solar heating of the Andes.

4. Numerical solution for the case of a nonisentropic lower boundary

The analytical solutions discussed in section 3 are for the special case in which the topographic surface is also an isentropic surface. When isentropic surfaces intersect the topographic surface, they can be considered to run along the topographic surface with a pressure equal to the surface pressure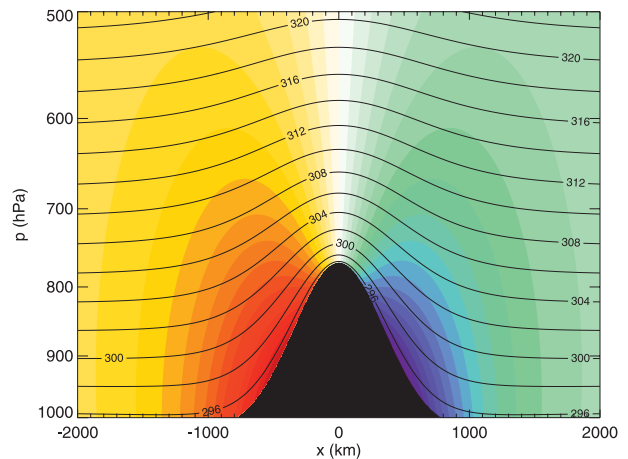, thereby forming a massless layer with infinite potential vorticity (i.e., $\partial p/\partial\theta \rightarrow 0$ and $P \rightarrow \infty$). Lorenz (1955) was the first to define a massless layer, not in the context of potential vorticity dynamics but in the context of available potential energy. Later, Bretherton (1966) showed that a potential temperature gradient along a boundary could be replaced by a boundary with constant potential temperature provided a concentration of potential vorticity very close to the surface is included. The Bretherton concept of a dynamical massless layer has been used in many later studies (e.g., Hoskins et al. 1985; Thorpe 1985, 1986; Andrews 1983; Fulton and Schubert 1991; Schneider et al. 2003; Schneider 2005). The isentropic surface that is just at the earth's surface over both the topographic feature and in the far field is labeled $\theta = \theta_B$. Then, defining $\theta_S(x)$ as the actual value of potential temperature on the topographic surface, the region $\theta_B \leq \theta < \theta_S(x)$ is the massless layer. When there is a massless layer, the $1/P$ factor in the first term of (2) takes on the value of zero (i.e., $P \rightarrow \infty$) in the massless layer. This introduces a variable coefficient effect that removes the advantages of using Fourier transforms. Thus, in this section, we solve a discretized (finite difference) version of the invertibility problem using an iterative method. In particular, we shall obtain solutions for the second and third cases shown schematically in Fig. 4.

When the invertibility principle is solved using finite difference methods rather than Fourier transform methods, it is unnecessary to separate the fields into a far-field part and a deviation part, as was done in section 3. Thus, returning to (2) and making use of the geostrophic relation $fv = (\partial M/\partial x)$ and the hydrostatic relation $\Pi = (\partial M/\partial\theta)$, we obtain (22) below, where the density ρ is given in terms of M by (23). Note that the appearance of ρ (as opposed to $\tilde{\rho}$) in the top line of (22) retains the previously discussed weak nonlinearity, which is easily
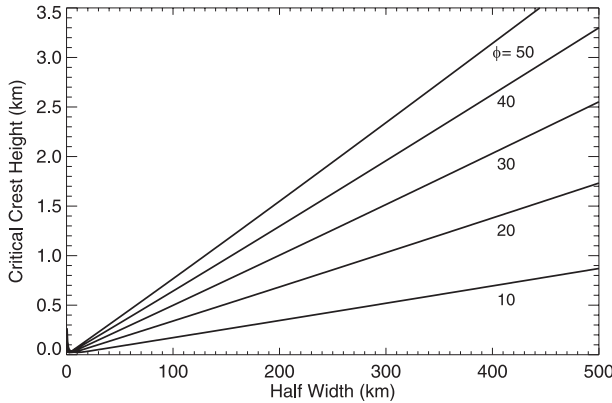
FIG. 8. Critical height H_{crit} of a Gaussian mountain as a function of width at five latitudes.

incorporated into the iterative method. The top line of (22) holds above the massless layer, while in the massless layer $P \to \infty$ and the top line reduces to the bottom line of (22). To obtain the lateral boundary conditions (24) we have assumed that the far-field (i.e., $x = \pm L$) value of M is equal to the specified function $\tilde{M}(\theta)$. To obtain the upper boundary condition (25) we have assumed that the upper isentropic surface ($\theta = \theta_T$) is also an isobaric surface with a constant Exner function Π_T. To formulate the lower boundary condition (26) we have applied the general relation $M - \theta(\partial M/\partial \theta) = \phi$ at $\theta = \theta_B$. In summary, the elliptic problem is

$$\frac{g}{f\theta\rho P}\left(f^2 + \frac{\partial^2 M}{\partial x^2}\right) + \frac{\partial^2 M}{\partial \theta^2} = 0 \quad \text{for} \quad \theta_S(x) < \theta \leq \theta_T,$$
$$\frac{\partial^2 M}{\partial \theta^2} = 0 \quad \text{for} \quad \theta_B \leq \theta < \theta_S(x),$$
$$(22)$$

$$\rho = \frac{p_0}{R\theta}\left(\frac{1}{c_p}\frac{\partial M}{\partial \theta}\right)^{c_v/R}, \tag{23}$$

$$M = \tilde{M}(\theta) \quad \text{at} \quad x = \pm L, \tag{24}$$

$$\frac{\partial M}{\partial \theta} = \Pi_T \quad \text{at} \quad \theta = \theta_T, \tag{25}$$

$$M - \theta\frac{\partial M}{\partial \theta} = \phi_S(x) \quad \text{at} \quad \theta = \theta_B, \tag{26}$$

where $c_v = c_p - R$ is the specific heat at constant volume.

To solve (22)–(26) for $M(x, \theta)$, we must specify the constants θ_B, θ_T, Π_T, and L and the functions $P(x, \theta)$, $\theta_S(x)$, $\phi_S(x)$, and $\tilde{M}(\theta)$. In section 3 we assumed that $\theta_S(x)$ was equal to the constant θ_B, so there was no massless layer. We also assumed that $P(x, \theta) = \tilde{P}(\theta)$, so

the potential vorticity did not vary along θ surfaces. With these assumptions, the interior anticyclonic flow was determined entirely by $\phi_S(x)$ and $\tilde{M}(\theta)$.

Now consider the more general case where $\theta_S(x) \neq \theta_B$, $\phi_S(x) \neq 0$, $P(x, \theta) = \tilde{P}(\theta)$ for $\theta_S(x) < \theta \leq \theta_T$, but $P(x, \theta) \to \infty$ for $\theta_B \leq \theta < \theta_S(x)$. In this case there is a massless layer on the mountain slope. However, even in this case there is a resting, horizontally homogeneous solution if the functions $\theta_S(x)$, $\phi_S(x)$, and $\tilde{M}(\theta)$ are specified in a particular way. This particular specification can be obtained by simply noting that $M(x, \theta) = \tilde{M}(\theta)$ for $\theta_S(x) < \theta \leq \theta_T$ is a resting solution. The Exner function and the geopotential associated with this solution are $\Pi(x, \theta) = \tilde{\Pi}(\theta)$ and $\phi(x, \theta) = \tilde{\phi}(\theta)$. If this geopotential field is to match the topography, we must have

$$\phi_S(x) = \tilde{\phi}[\theta_S(x)]. \tag{27}$$

In other words, if $\phi_S(x)$, $\theta_S(x)$, and $\tilde{\phi}(\theta)$ are specified in such a way that (27) is satisfied, the solutions of the elliptic problem (22)–(26) are $v(x, \theta) = 0$ and $\Pi(x, \theta) = \tilde{\Pi}(\theta)$ for $\theta_S(x) < \theta \leq \theta_T$. For the far-field profile specified by (10) and the Gaussian mountain specified by (16), the constraint (27) can be rearranged to

$$\theta_S(x) = \theta_B\left(1 + \frac{2N^2H}{g}e^{-x^2/a^2}\right)^{1/2}. \tag{28}$$

This argument provides us with a useful check on any numerical procedure for solving (22)–(26). This "null" test case will be discussed later (Fig. 9). It is interesting to note that even in this test case the wind field in the massless layer does not vanish.

To discretize the problem (22)–(26) we introduce the grid points $(x_j, \theta_k) = (-L + j\Delta x, \theta_B + k\Delta\theta)$ with $j = 0, 1, \ldots, J$ and $k = 0, 1, \ldots, K$, where $\Delta x = 2L/J$ and $\Delta\theta = (\theta_T - \theta_B)/K$. Then we seek an approximate solution with gridpoint values $M_{j,k}$ satisfying the discrete equation

$$A_{j,k}[(f\Delta x)^2 + M_{j-1,k} - 2M_{j,k} + M_{j+1,k}]$$
$$+ M_{j,k-1} - 2M_{j,k} + M_{j,k+1} = 0, \tag{29}$$

where the dimensionless coefficient $A_{j,k}$ is defined by

$$A_{j,k} = \frac{g(\Delta\theta)^2}{f\theta_k\rho_{j,k}P_{j,k}(\Delta x)^2}. \tag{30}$$

The discretized versions of (25) and (26) are

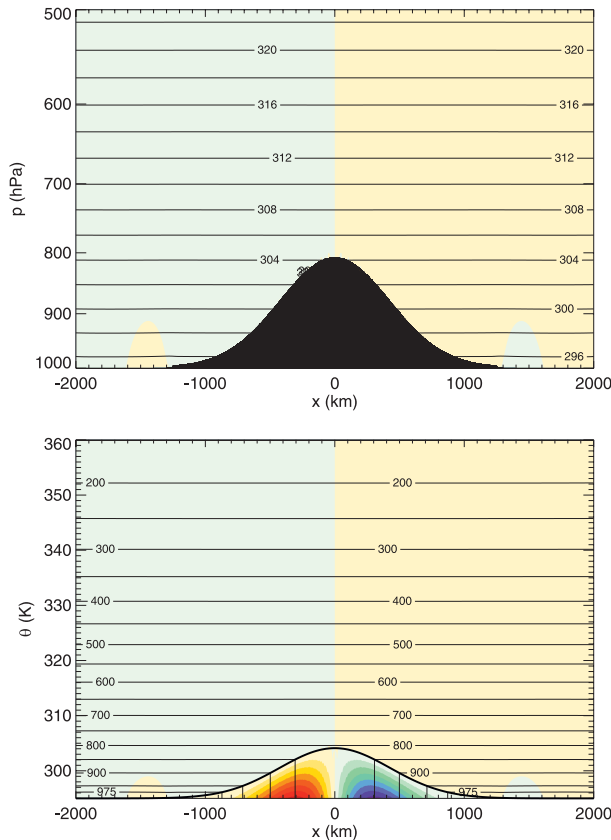$$M_{j,K} - M_{j,K-1} = \Pi_T\Delta\theta, \tag{31}$$

FIG. 9. A null case (i.e., no flow) in which $\tilde{\phi}(\theta)$, $\phi_S(x)$, and $\theta_S(x)$ are specified such that (27) is satisfied. In this particular null case, $\tilde{\phi}(\theta)$ is given by (10), $\phi_S(x)$ by (16), and $\theta_S(x)$ by (28). Black contours are (top) isentropes and (bottom) isobars. The anticyclone in the massless layer of the bottom panel (below the thick black line) is not apparent in the top panel because the massless layer has "zero thickness" in (x, p) space.

$$M_{j,0} - \frac{\theta_B}{\Delta\theta}(M_{j,1} - M_{j,0}) = \phi_S(x_j). \quad (32)$$

Note that (29) applies both outside and inside the massless layer, with $A_{j,k} \neq 0$ outside the massless layer and $A_{j,k} = 0$ inside the massless layer. Also note that the problem is nearly isotropic on the grid outside the massless layer if $A_{j,k} \approx 1$, which can serve as a rough guide for the choice of the ratio $\Delta\theta/\Delta x$. Using typical values of the quantities on the rhs of (30), we obtain the rough guide $(\Delta\theta/\Delta x) \approx (1 \text{ K})/(57 \text{ km})$. For the numerical solutions presented here, we have chosen $\Delta x = 8$ km and $\Delta\theta = 65/450 = 0.144\overline{4}$ K, resulting in a grid with $J = 750$ and $K = 450$ for the domain $-3000 \leq x \leq 3000$ km and $295 \leq \theta \leq 360$ K.

We solve the discrete equations (29)–(32) using the following successive overrelaxation (SOR) procedure. Denoting the current estimate of $M_{j,k}$ by $\hat{M}_{j,k}$ (not to be confused with the "hat" notation in section 3 to denote

the Fourier component of a variable), and sweeping through the grid in lexicographic order, we first compute the current estimate of density from

$$\hat{\rho}_{j,k} = \frac{p_0}{R\theta_k}\left(\frac{\hat{M}_{j,k+1} - \hat{M}_{j,k-1}}{c_p 2\Delta\theta}\right)^{c_v/R}, \quad (33)$$

the current estimate of the dimensionless coefficient from

$$\hat{A}_{j,k} = \begin{cases} \dfrac{g(\Delta\theta)^2}{f\theta_k\hat{\rho}_{j,k}P_{j,k}(\Delta x)^2} & \text{if} \quad \theta_S(x_j) < \theta_k < \theta_T \\ 0 & \text{if} \quad \theta_B < \theta_k < \theta_S(x_j) \end{cases} \quad (34)$$

and then the current residual from

$$\hat{r}_{j,k} = \hat{M}_{j,k-1} + \hat{M}_{j,k+1} - 2(1 + \hat{A}_{j,k})\hat{M}_{j,k} + \hat{A}_{j,k}[(f\Delta x)^2 + \hat{M}_{j-1,k} + \hat{M}_{j+1,k}]. \quad (35)$$

The solution estimate is then updated by

$$\hat{M}_{j,k} \leftarrow \hat{M}_{j,k} + \frac{\omega\hat{r}_{j,k}}{2(1 + \hat{A}_{j,k})}, \quad (36)$$

where ω is the overrelaxation factor and (35) and (36) are computed at the grid points $1 \leq j \leq J - 1$, $1 \leq k \leq K - 1$. Finally, the top and bottom boundary points are updated from the boundary conditions (31) and (32), written in the form

$$\hat{M}_{j,K} \leftarrow \hat{M}_{j,K-1} + \Pi_T\Delta\theta \quad \text{for} \quad 1 \leq j \leq J - 1, \quad (37)$$

$$\hat{M}_{j,0} \leftarrow \frac{(\theta_B/\Delta\theta)\hat{M}_{j,1} + \phi_S(x_j)}{1 + (\theta_B/\Delta\theta)} \quad \text{for} \quad 1 \leq j \leq J - 1. \quad (38)$$

Equations (33)–(38) are iterated, starting with the initial estimate $\hat{M}_{j,k} = \tilde{M}(\theta_k)$. This initial estimate does not change on the lateral boundaries $j = 0, J$. To gauge the convergence rate, we have monitored the norm of the residual as iteration proceeds. Experience shows that, when this norm has decreased by approximately two orders of magnitude, the wind field no longer significantly changes with further iterations. All of the figures shown have been iterated until the residual has decreased by more than two orders of magnitude. Based on numerical tests, overrelaxation factors between 1.70 and 1.95 have been used.

The above iterative procedure determines the Montgomery potential in the entire domain for a given surface geopotential $\phi_S(x)$, a given surface potential temperature
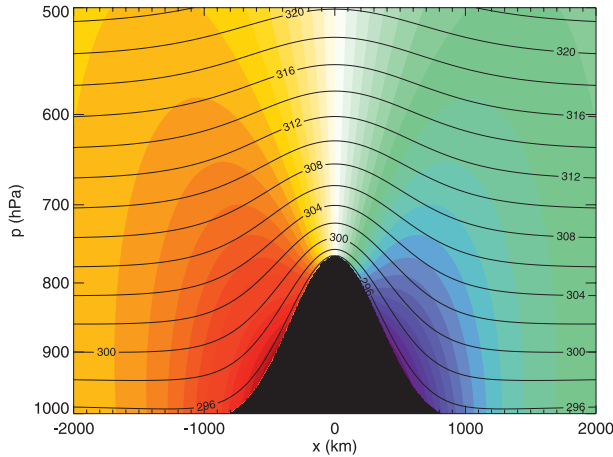
FIG. 10. Meridional wind field (shading, warm colors are positive and cool colors negative; the contour interval is 1 m s^{-1}) for an isentropic lower boundary computed using SOR. The maximum height of the Gaussian mountain is 2500 m and its width $a = 500$ km. The maximum winds are ± 21.0 m s^{-1}.

$\theta_S(x)$, and a given $\tilde{M}(\theta)$. From the Montgomery potential, the wind field can be easily recovered using geostrophic balance, and the pressure field can be computed using the hydrostatic approximation. As a "null" test of this numerical procedure, we have specified $\tilde{M}(\theta)$ according to (9), $\phi_S(x)$ according to (16), and $\theta_S(x)$ according to (28). This combination should result in no flow and a horizontally homogeneous mass field outside the massless layer. The numerical solution is shown in Fig. 9, which agrees well with the expected result. Note that, when the solution is displayed in (x, θ) space (bottom panel of Fig. 9), there is an anticyclonic flow confined entirely to the massless layer. This anticyclone does not appear when the solution is displayed in (x, p) space (top panel).

Figure 10 shows the solution computed for an isentropic ridge of the same height (2500 m) as the ridge shown in Fig. 7. A comparison of these two figures shows that the solution derived using Fourier transforms (Fig. 7) and the solution found with the above iterative procedure (Fig. 10) are similar, but the maximum winds in Fig. 10 are 1.8 m s^{-1} stronger than those in Fig. 7. These figures are not expected to be identical because Fig. 7 was computed assuming the density was equal to the far-field density (which depends only on θ) while Fig. 10 was computed with density as a function of x and θ. The difference between Figs. 7 and 10 is primarily due to the difference in the rhs of (6). Figure 7 results from the assumptions $(\tilde{\rho}/\rho) \to 1$ and $(\tilde{P}/P) \to 1$ so that the rhs of (6) vanishes. Figure 10 results from the assumption $(\tilde{P}/P) \to 1$, so that the rhs of (6) becomes $f(\tilde{\rho}/\rho)[(\rho/\tilde{\rho}) - 1]$, which is negative near the mountain crest since $\rho < \tilde{\rho}$ there. This negative rhs of (6) leads to a slightly stronger
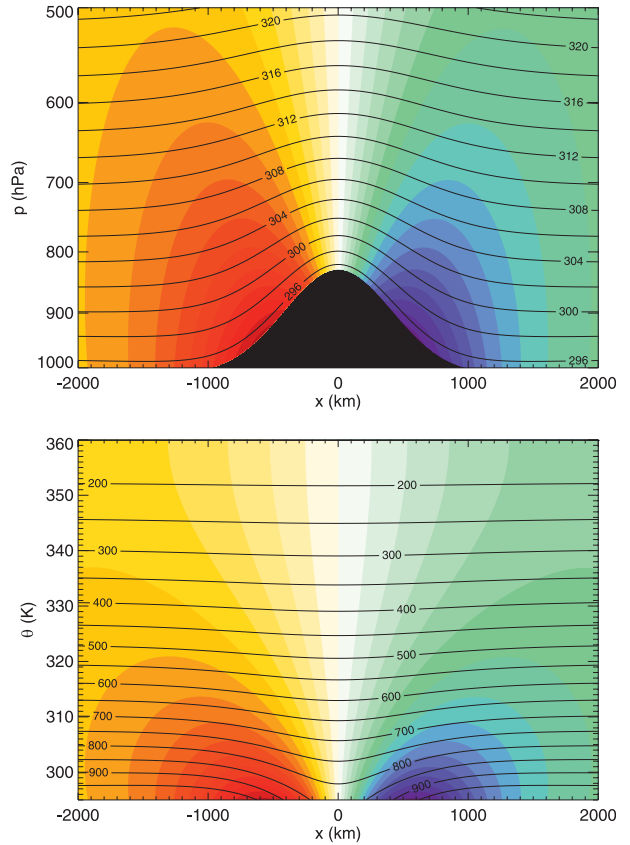

FIG. 11. Meridional wind field (shading, 1 m s^{-1} interval) for an isentropic ridge with $H = 1800$ m and a Gaussian width $a = 600$ km. The flow is anticyclonic with $v_{max} = \pm 15.4$ m s^{-1}. Black contours are (top) isentropes and (bottom) isobars.

anticyclone in Fig. 10 compared to Fig. 7. Note that the errors caused by the assumption $(\tilde{\rho}/\rho) \to 1$ are expected to be less for cases in which the crest height is much smaller than the critical crest height.

Figures 11–14 show the wind fields that result from the simple cases represented schematically in Fig. 4. An isentropic ridge with a crest height of 1800 m is shown in Fig. 11 and can be clearly identified by the fact that the isentropes do not intersect the ridge and the flow is anticyclonic. A flat lower boundary with a surface potential temperature anomaly of 6 K is shown in Fig. 12, which results in a 12.7 m s^{-1} cyclonic flow. Figure 13 combines these two forcing cases into a warm ridge with a crest height of 1800 m and a surface potential temperature anomaly of 6 K. Note that the isentropic lower surface (Fig. 11) has anticyclonic flow anchored over the ridge, but for the case of the flat lower boundary (Fig. 12) the flow is cyclonic. The warm ridge with a surface potential temperature anomaly of 6 K has anticyclonic flow (Fig. 13), but when the surface potential temperature anomaly is increased to 12 K (Fig. 14), the flow becomes
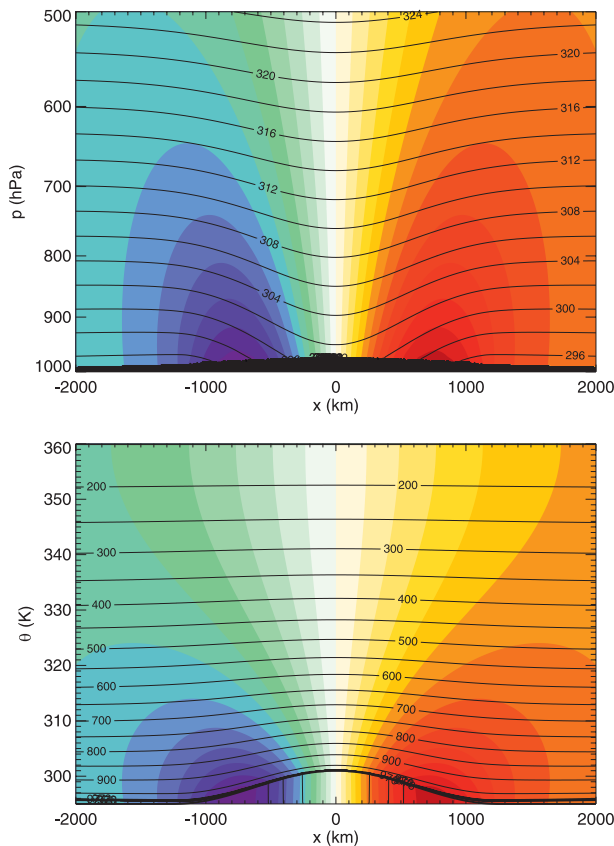
FIG. 12. Meridional wind field (shading, 1 m s^{-1} interval) for a flat lower surface having a 6-K warm potential temperature anomaly. The resulting winds have $v_{max} = \pm 12.7$ m s^{-1}. The massless layer is indicated (top) in (x, p) space by the black region along the lower boundary and (bottom) in (x, θ) space by the thick black line. Contour spacing for the pressure field in the massless layer is 1 hPa.
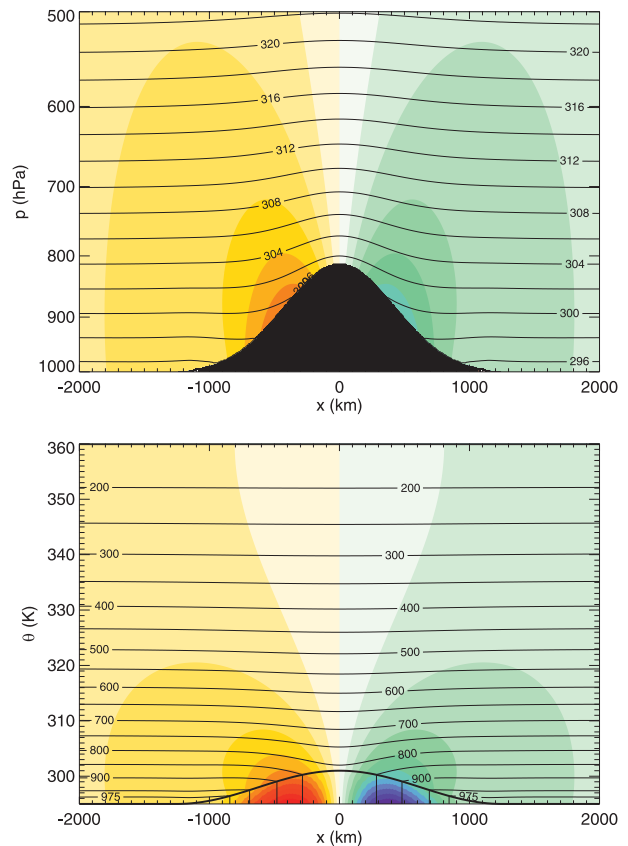
FIG. 13. Meridional wind field (shading, 1 m s^{-1} interval) for a heated ridge with a 6-K warm potential temperature anomaly, $a = 600$ km, $H = 1800$ m, and $v_{max} \approx \pm 5$ m s^{-1} (above the massless layer). The massless layer is indicated by (top) the black region and (bottom) the thick black line. Contour spacing of isobars (bottom) is 50 hPa except for lowest contour of 975 hPa.

cyclonic and resembles more closely the flow structures seen in Fig. 2. This demonstrates the competing influences of the purely orographic forcing and the surface thermal forcing. Once the surface potential temperature anomaly has grown strong enough to overcome the anticyclonic flow associated with an isentropic obstacle, the wind field produced by a warm ridge becomes cyclonic and strengthens as the surface potential temperature anomaly strengthens. It can also be shown that as the width of the ridge increases for a given potential temperature anomaly, the influence of the anomaly is spread out and effectively acts as a weaker anomaly.

It is also apparent in (x, θ) space that the isentropic ridge case does not contain a massless layer, but for the warm flat lower boundary (Fig. 12) and the warm ridge (Figs. 13 and 14) a massless layer is present and marked as the area below the thick black "surface" line. Pressure in the massless layer is independent of θ, as is clear

from the vertical isobars within the massless layers of Figs. 12–14. Although the pressure is independent of θ in the massless layer, it does vary with x, resulting in a nonzero wind field. The pressure and wind fields in the massless layer do not have direct physical meaning. They can be simply regarded as a consequence of formulating (and discretizing) the invertibility principle on a domain (and grid) that is uniform in (x, θ) space, even though θ is not uniform on the lower boundary.

For the case of an isentropic lower boundary the potential vorticity is uniform on each θ surface. This leads to a simple explanation for the wind field response to the mountain as seen in Figs. 6, 7, and 10. Recall that, for adiabatic flows, mass cannot cross isentropic surfaces, which constrains how the mass field can adjust when the isentropes are moved up or down. One of the primary benefits of using isentropic coordinates is the simplicity of the expression for potential vorticity. The denominator of the potential vorticity is given by the pseudodensity
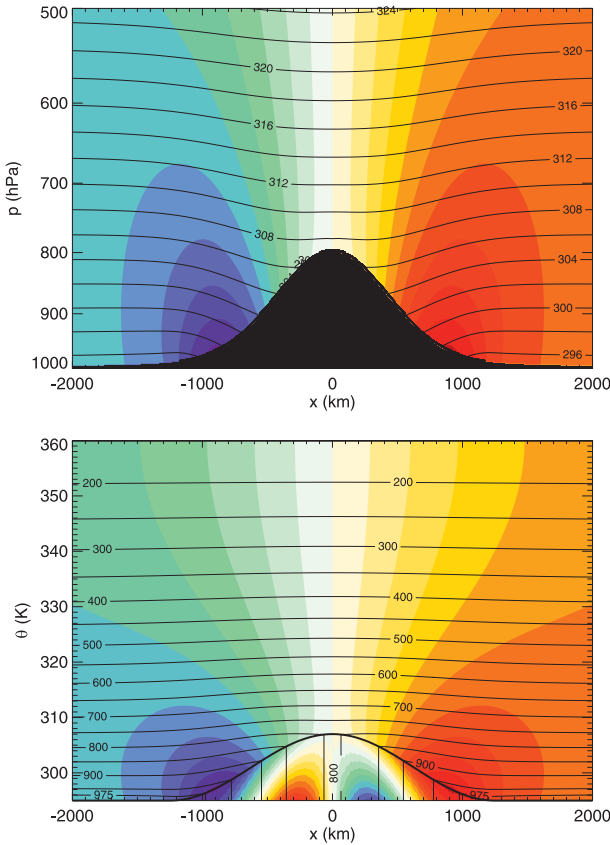
FIG. 14. As in Fig. 13, but with a 12-K warm potential temperature anomaly. The isentropes now bend down toward higher pressure and the flow is cyclonic with $v_{\max} = \pm 10.3 \text{ m s}^{-1}$.

$-(1/g)(\partial p/\partial \theta)$, which becomes smaller when the isentropes are compressed, as occurs over the crest of an isentropic ridge. Because the potential vorticity is uniform, the decrease in magnitude of the denominator implies the numerator also must decrease. The only part of the numerator that can decrease in magnitude is $\partial v/\partial x$, so a negative isentropic relative vorticity is required, which is exactly what Figs. 6, 7, and 10 show. It is apparent that the velocity gradient is greatest where the isentropes are the most compressed. Similar reasoning can be applied to the case of stretched isentropes with the only difference being the sign of the isentropic relative vorticity.

The structure of the isentropes for the case with a sufficiently warm mountain crest (Fig. 14) is quite different. Near the mountain the isentropes bend downward toward the warm mountain crest. Isentropes that intersect the mountain can be considered to run along the mountain crest until they erupt on the other side of the mountain. With this interpretation, there is an infinitesimally thin massless layer of infinite PV on the mountain crest. Then, by the invertibility principle and with uniform PV along isentropes that do not intersect the mountain, there

is a cyclonic flow with a low-level jet on each side of the mountain.

Each of Figs. 11–14 shows the wind maxima to be in the lowest layers of the fluid and to decay rapidly in the vertical and horizontal directions. This matches fairly well with the basic characteristics of observed low-level jets, although inclusion of surface frictional and boundary layer effects in the theoretical argument is probably necessary for accurate placement of the height of the jet maxima. In agreement with the insights offered by the invertibility principle, these figures show increased (decreased) mountain top vorticity when the isentropes are stretched (compressed). These figures clearly indicate that in the absence of other factors a sufficiently warm mountain crest will result in a cyclonic wind field. It is also clear that the jets of opposite sign on either side of the ridge are two parts of the response to the forcing (i.e., a sufficiently warm ridge leads to a pair of LLJs that form a cyclonic couplet). Finally, it is important to remember that the balanced potential vorticity arguments given here apply to the time-averaged flow and that there are important superimposed diurnal oscillations (not accurately captured by PV invertibility arguments) of the type studied by Blackadar (1957), Holton (1967), and Jiang et al. (2007).

5. Concluding remarks

The results presented here show that the thin sheet of surface potential vorticity that is the result of the potential temperature anomalies along the heated topography plays a key role in the dynamics of atmospheric low-level jets. This conclusion has been reached by solving the invertibility principle for the balanced response of a stratified fluid to forcing along the lower boundary. Figure 4 schematically represents the three types of lower boundary forcing we have studied here: an isentropic ridge along the lower boundary, in which case $\phi_S(x) \neq 0$ and $\theta_S(x) = \theta_B$; a locally heated, flat lower boundary, in which case $\phi_S(x) = 0$ and $\theta_S(x) \neq \theta_B$; and a heated ridge, in which case $\phi_S(x) \neq 0$ and $\theta_S(x) \neq \theta_B$. Isentropic ridges produce an anticyclonic wind field. The closer the crest height comes to the critical crest height, the tighter the isentropes are packed over the ridge and the stronger the corresponding wind field. In contrast, the case of a locally heated flat lower boundary results in a cyclonic wind field. When these two cases are combined into the case of a heated ridge, the winds are reduced due to the competing effects of the orography (ϕ_S) and the heating (θ_S). For small potential temperature anomalies on the surface, the influence of ϕ_S is dominant and the wind field is anticyclonic. However, for surface potential temperature anomalies that are larger and closer to those observed in

YOTC, the heating along the lower boundary is the dominant effect, and the wind field is cyclonic. As an example of these competing effects, the case shown in Fig. 13, with a surface potential temperature anomaly of 6 K, has an anticyclonic flow, while the case shown in Fig. 14, with a surface potential temperature anomaly of 12 K, has a cyclonic flow. Byerle and Paegle (2003) have discussed the seasonal transition from cyclonic to anticyclonic flow in the context of the Great Plains low-level jet. The results presented here suggest that this seasonal transition is due to the fall potential temperature anomaly dropping below the critical value that is needed for a cyclonic circulation.

Past studies of the South American LLJ (Vera et al. 2006) and the Chilean coastal LLJ (Jiang et al. 2010) have treated these jets as isolated phenomena. This viewpoint also dominates studies of the LLJs in North America (see Holton 1967; Blackadar 1957; Wexler 1961; Jiang et al. 2007, etc.). The results presented here clearly show that these pairs of LLJs can be attributed to the PV anomaly that is generated by heating of the elevated terrain. Although we have only treated $\phi_S(x)$ and $\theta_S(x)$ functions that are symmetric about $x = 0$, the YOTC observations shown in Figs. 1–3 indicate that surface potential temperatures are colder on the west side owing to upwelling in the eastern Pacific Ocean. Incorporation of this asymmetry into the specified $\theta_S(x)$ leads to a corresponding asymmetry in the LLJs (i.e., a stronger Chilean LLJ).

Two limiting aspects of the present work are the f-plane and y-independent assumptions. This raises the obvious question as to whether it is possible to generalize the present theory to balanced flows on the sphere. Such a generalization has been given by Silvers (2011). The specified topography and the specified potential temperature on the lower boundary are then given by $\phi_S(\lambda, \mu)$ and $\theta_S(\lambda, \mu)$, where λ is the longitude and μ is the sine of the latitude. The relation between the mass field and the wind field is assumed to be the local linear balance (Schubert et al. 2009) condition $M(\lambda, \mu, \theta) = 2\Omega\mu\psi(\lambda, \mu, \theta)$, where $\psi(\lambda, \mu, \theta)$ is the streamfunction for the nondivergent (i.e., zero isentropic divergence) part of the flow. Then, the spherical generalization of (22) is

$$\frac{g}{\theta \rho P}(2\Omega\mu + \nabla^2\psi) + 2\Omega\mu\frac{\partial^2\psi}{\partial\theta^2} = 0$$
$$\text{for}\quad \theta_S(\lambda, \mu) < \theta \leq \theta_T,$$
$$2\Omega\mu\frac{\partial^2\psi}{\partial\theta^2} = 0 \quad\text{for}\quad \theta_B \leq \theta < \theta_S(\lambda, \mu), \qquad (39)$$

where ∇^2 is the two-dimensional (fixed θ) Laplacian operator on the sphere. With appropriate boundary conditions, (39) constitutes an invertibility principle for topographically bound flows on the sphere. Solution of this three-dimensional elliptic problem allows treatment of much more realistic topography $\phi_S(\lambda, \mu)$ than was treated in sections 3 and 4.

APPENDIX

Analytic Solution Using Fourier Integral Transforms

To solve the invertibility problem (11)–(15) we use Fourier integral transforms. For simplicity we assume that the specified function $\phi_S(x)$ is symmetric in x so that $\Pi'(x, \theta)$ is symmetric in x and $v(x, \theta)$ is antisymmetric in x. The Fourier sine transform pair for $v(x, \theta)$ is

$$\hat{v}(k, \theta) = \frac{2}{\pi}\int_0^\infty v(x, \theta)\sin(kx)\,dx, \qquad (A1)$$

$$v(x, \theta) = \int_0^\infty \hat{v}(k, \theta)\sin(kx)\,dk, \qquad (A2)$$

while the Fourier cosine transform pair for $\Pi'(x, \theta)$ is

$$\hat{\Pi}'(k, \theta) = \frac{2}{\pi}\int_0^\infty \Pi'(x, \theta)\cos(kx)\,dx, \qquad (A3)$$

$$\Pi'(x, \theta) = \int_0^\infty \hat{\Pi}'(k, \theta)\cos(kx)\,dk. \qquad (A4)$$

A similar cosine transform pair exists for the surface geopotential $\phi_S(x)$ and its transform $\hat{\phi}_S(k)$.

We now wish to Fourier transform (11), (12), (14), and (15). To Fourier transform (11) and (14) we multiply them by $\cos(kx)$ and integrate over x from 0 to ∞, thereby obtaining (A5) and (A7) below. To Fourier transform (12) and (15) we multiply them by $\sin(kx)$ and integrate over x from 0 to ∞, thereby obtaining (A6) and

(A8) below. In summary, the Fourier transform of the elliptic problem (11)–(15) is

$$k\hat{v} + \left(\frac{f\theta_B^2 N_B^2}{g^2}\right)\frac{d\hat{\Pi}'}{d\theta} = 0, \qquad (A5)$$

$$f\frac{d\hat{v}}{d\theta} + k\hat{\Pi}' = 0 \qquad (A6)$$

with boundary conditions

$$\hat{\Pi}' = 0 \quad \text{at} \quad \theta = \theta_T, \qquad (A7)$$

$$\theta\frac{d\hat{v}}{d\theta} - \hat{v} = \frac{k}{f}\hat{\phi}_S(k) \quad \text{at} \quad \theta = \theta_B. \qquad (A8)$$

As can be confirmed by direct substitution, the solutions of (A5)–(A8) are[A1]

$$\hat{v}(k,\theta) = -\frac{k}{f}\hat{\phi}_S(k)\left[\frac{e^{-\kappa(\theta-\theta_B)} + e^{-\kappa(2\theta_T-\theta_B-\theta)}}{1 + \kappa\theta_B + (1 - \kappa\theta_B)e^{-2\kappa(\theta_T-\theta_B)}}\right], \qquad (A9)$$

$$\frac{\theta_B N_B}{g}\hat{\Pi}'(k,\theta) = -\frac{k}{f}\hat{\phi}_S(k)$$
$$\times\left[\frac{e^{-\kappa(\theta-\theta_B)} - e^{-\kappa(2\theta_T-\theta_B-\theta)}}{1 + \kappa\theta_B + (1 - \kappa\theta_B)e^{-2\kappa(\theta_T-\theta_B)}}\right], \qquad (A10)$$

where $\kappa(k) = gk/(f\theta_B N_B)$. The Fourier cosine transform of (16) yields

$$\hat{\phi}_S(k) = \frac{gHa}{\sqrt{\pi}}e^{-a^2k^2/4}. \qquad (A11)$$

Using (A9), (A10), and (A11) in (A2) and (A4), we obtain the final solutions (17) and (18).

REFERENCES

Andrews, D. G., 1983: A finite-amplitude Eliassen–Palm theorem in isentropic coordinates. *J. Atmos. Sci.,* **40,** 1877–1883.

Blackadar, A. K., 1957: Boundary layer wind maxima and their significance for the growth of nocturnal inversions. *Bull. Amer. Meteor. Soc.,* **38,** 283–290.

Bonner, W. D., 1968: Climatology of the low level jet. *Mon. Wea. Rev.,* **96,** 833–850.

Bretherton, F. P., 1966: Critical layer instability in baroclinic flows. *Quart. J. Roy. Meteor. Soc.,* **92,** 325–334.

Byerle, L. A., and J. Paegle, 2002: Description of the seasonal cycle of low-level flows flanking the Andes and their interannual variability. *Meteorológica,* **27,** 71–88.

——, and ——, 2003: Modulation of the Great Plains low-level jet and moisture transports by orography and large-scale circulations. *J. Geophys. Res.,* **108,** 8611, doi:10.1029/2002JD003005.

Eliassen, A., 1980: Balanced motion of a stratified, rotating fluid induced by bottom topography. *Tellus,* **32,** 537–547.

Fulton, S. R., and W. H. Schubert, 1991: Surface frontogenesis in isentropic coordinates. *J. Atmos. Sci.,* **48,** 2534–2541.

Holton, J. R., 1967: The diurnal boundary layer wind oscillation above sloping terrain. *Tellus,* **19,** 199–205.

Hoskins, B. J., M. E. McIntyre, and A. W. Robertson, 1985: On the use and significance of isentropic potential vorticity maps. *Quart. J. Roy. Meteor. Soc.,* **111,** 877–946.

Jiang, Q., S. Wang, and L. O'Neill, 2010: Some insights into the characteristics and dynamics of the Chilean low-level coastal jet. *Mon. Wea. Rev.,* **138,** 3185–3206.

Jiang, X., N.-C. Lau, I. M. Held, and J. J. Ploshay, 2007: Mechanisms of the Great Plains low-level jet as simulated in an AGCM. *J. Atmos. Sci.,* **64,** 532–547.

Lorenz, E. N., 1955: Available potential energy and the maintenance of the general circulation. *Tellus,* **7,** 157–167.

Rife, D. L., J. O. Pinto, A. J. Monaghan, C. A. Davis, and J. R. Hannan, 2010: Global distribution and characteristics of diurnally varying low-level jets. *J. Climate,* **23,** 5041–5064.

Schneider, T., 2005: Zonal momentum balance, potential vorticity dynamics, and mass fluxes on near-surface isentropes. *J. Atmos. Sci.,* **62,** 1884–1900.

——, I. M. Held, and S. T. Garner, 2003: Boundary effects in potential vorticity dynamics. *J. Atmos. Sci.,* **60,** 1024–1040.

Schubert, W. H., R. K. Taft, and L. G. Silvers, 2009: Shallow water quasi-geostrophic theory on the sphere. *J. Adv. Model. Earth Syst.,* **1** (2), doi:10.3894/JAMES.2009.1.2.

Silvers, L. G., 2011: A theory of topographically bound balanced motions and application to atmospheric low-level jets. Ph.D. dissertation, Colorado State University, 78 pp.

Stensrud, D. J., 1996: Importance of low-level jets to climate: A review. *J. Climate,* **9,** 1698–1711.

Thorpe, A. J., 1985: Diagnosis of balanced vortex structure using potential vorticity. *J. Atmos. Sci.,* **42,** 397–406.

——, 1986: Synoptic scale disturbances with circular symmetry. *Mon. Wea. Rev.,* **114,** 1384–1389.

Ting, M., and H. Wang, 2006: The role of the North American topography on the maintenance of the Great Plains summer low-level jet. *J. Atmos. Sci.,* **63,** 1056–1068.

Vera, C., and Coauthors, 2006: The South American low-level jet experiment. *Bull. Amer. Meteor. Soc.,* **87,** 63–77.

Waliser, D. E., and Coauthors, 2012: The ''year'' of tropical convection (May 2008 to April 2010): Climate variability and weather highlights. *Bull. Amer. Meteor. Soc.,* **93,** 1189–1218.

Wexler, H., 1961: A boundary layer interpretation of the low-level jet. *Tellus,* **13,** 368–378.

[A1] The solutions of (A5)–(A8) can also be expressed in terms of $\cosh(\kappa\theta)$ and $\sinh(\kappa\theta)$, but for large horizontal wavenumbers, numerical evaluation of the hyperbolic representation of the solution presents a practical difficulty since the ratio of very large numbers is involved. This difficulty does not occur in the exponential representation (A9) and (A10) since this representation avoids evaluation of exponential functions with large positive exponents.